Bridging Li-Ion Batteries and Fuel Cells: from Cathode Leaching Residue to Atomic-Scale Catalytic System

Mengjie Liu,[a,†] Tsung-Cheng Yang,[b,†] Zhefei Pan,[c] Jeongyeon Lee,[a] Liang An,[c] Baolong Qiu,[d] Huayi Yin,[d,e] Chia-Min Yang,[b,] and Lawrence Yoon Suk Lee[a,*]*

a Department of Applied Biology and Chemical Technology and Research Institute for Smart Energy, The Hong Kong Polytechnic University, Hung Hom, Kowloon, Hong Kong SAR, China

b Department of Chemistry, National Tsing Hua University, Hsinchu 300034, Taiwan

c Department of Mechanical Engineering, The Hong Kong Polytechnic University, Hung Hom, Kowloon, Hong Kong SAR, China

d Key Laboratory for Ecological Metallurgy of Multimetallic Mineral of Ministry of Education, School of Metallurgy, Northeastern University, Shenyang, 110819, P. R. China

e School of Resource and Environmental Science, Wuhan University, Wuhan, 430072, P. R. China

AUTHOR INFORMATION

† M. L. and T.-C. Y contributed equally to this work.

Corresponding Authors

* Chia-Min Yang: cmyang@mx.nthu.edu.tw

* Lawrence Yoon Suk Lee: lawrence.ys.lee@polyu.edu.hk

ABSTRACT: End-of-life lithium-ion batteries (LIBs) constitute an "urban mine" that offers a great opportunity to repurpose the metal species. However, the direct and cross-domain reuse of their functional materials has been ignored. Herein, we report a case study of upcycling a LIB cathode, $LiFePO_4$ particles embedded in N-doped carbon spheres (LFP/C), to a single-atomic (SA) electrocatalyst for oxygen reduction reaction (ORR). Using a top-down leaching method, the LFP/C was converted to Fe SAs-embedded hollow carbon spheres containing minor FeO_x nanoclusters and $FePO_4$ nanoparticles ($SA_{Fe}/FeO_x/FePO_4$). Our studies indicate that the neighboring $FeO_x/FePO_4$ modulate the electronic filling in the antibonding state of SA_{Fe} sites and thereby optimize the intermediate adsorption energy at the rate-determining step, leading to the boosted half-cell ORR activity as manifested by a high E_{onset} of 0.97 V. Furthermore, the membrane electrode fabricated with the $SA_{Fe}/FeO_x/FePO_4$ demonstrates great potentials in two practical energy conversion devices, ammonia fuel cell and Zn–air battery, building a bridge across the energy applications.

TOC GRAPHICS

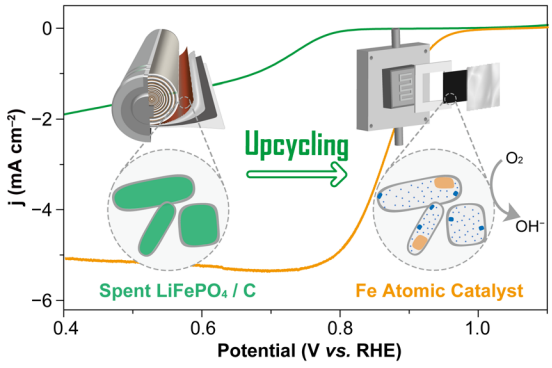

The shift in energy paradigm from fossil fuels to renewable energies has set a pressing demand for reliable technologies for energy conversion, and storage.[1] Lithium-ion batteries (LIBs) have gained a leading position in the market for electric vehicles and stationary energy storage grids, complementing renewable energy resources of an intermittent nature.[2] Given the exponential growth trajectory of the LIBs market, an ever-increasing quantity of spent LIBs would bring serious challenges for waste management and environment protection.[3] Compared with the conventional pyrometallurgical and hydrometallurgical method for LIBs recycling, a direct transformation of spent LIBs into advanced functional materials can avoid the energy-intensive yet inefficient steps of "recovery, purification, and synthesis", which is located at a higher position in the waste management hierarchy.[4-8]

Fuel cells (FCs) and Zn–air batteries (ZABs) are two other energy conversion devices that have shown compelling potential in powering electronic devices.[9-12] Although the electrochemical reactions occurring in these devices differ from those in LIBs, they share common features in the design principle towards the microstructure, surface/interface properties, and electronic/atomic configuration of electrode materials, suggesting an inherently close link between energy conversion and storage applications.[13-16] Given that sustainability can be counted as an extra dimension of an electrode in addition to its structure and property,[7] the fabrication of FC and/or ZAB electrodes using spent LIBs materials *via* simple modifications would represent a paradigm-shifting concept of upcycling that breaks the boundary of different technologies and improves the energy efficiencies in terms of both waste recycling and new device production.

The development of cost-effective oxygen reduction reaction (ORR) electrocatalysts is the key to the large-scale commercialization of FCs and ZABs.[17-19] Transition-metal single-atomic catalysts (SACs) have demonstrated excellent ORR performances owing to their unique merits of

high catalytic activity and maximum atomic utilization.[20-23] The rational design of SACs was usually accomplished by bottom-up approaches using organometallic precursors.[21, 22, 24] while the top-down strategy has rarely been considered due to the difficulty in atomic control.[23] However, spent LIBs cathode materials could offer an opportunity to construct SACs *via* the top-down leaching approach. The digested cathodes (*e.g.*, $LiCoO_2$, $LiMn_2O_4$, and $LiFePO_4$) can provide metal atoms for creating SA/cluster sites while the pyrolyzed carbon coatings of the cathode can serve as conductive supports to anchor metal species *via* the coordination with heteroatoms.[25]

Herein, we report the upcycling of the cathode material in spent LIBs into an active SA-based ORR catalyst using a simple leaching strategy. A previously reported LIB cathode, the carbon-encapsulated $LiFePO_4$ (LFP), was selected as a proof-of-concept model system and partially etched to an ensemble of Fe SAs (SA_{Fe}), nanoscale FeO_x clusters, and minor residual $FePO_4$ nanoparticles embedded in the hollow carbon sphere. Our characterizations indicate that the unsaturated O-coordinated SA_{Fe} sites from pristine FeO_6 octahedrons in LFP are highly active in catalyzing alkaline ORR, which is assisted by the synergistic effect of the nearby FeO_x cluster and $FePO_4$ particle. The hollow carbon wrapping the LFP core contributes to the catalysis by serving as the matrix to stabilize the surface-attached metal species by C–O bonding and facilitate electron transfer and electrolyte penetration. When employed as the membrane electrodes in ammonia FC and ZAB, the $SA_{Fe}/FeO_x/FePO_4$ catalyst shows superior peak power density and durability. This work points out the possibility of constructing SAC from waste LIBs cathode and demonstrates a new concept of cross-device LIBs upcycling.

Fig. S1 illustrates the overall upcycling of end-of-life $LiFePO_4$ batteries. After the preliminary treatments (**Scheme 1A**), $LiFePO_4$ encased in N-doped carbon (LFP/C) was extracted and immersed in HCl for partial etching, and the residual carbon-based precipitate was collected by

filtration and drying. The majority of Li and Fe contents that leached into HCl could be reclaimed by further solvent extraction and selective precipitation,[26] which is outside the scope of this study. The concentration of HCl and reaction time were carefully tuned to demonstrate the transition process of composition and chemical state of products during the etching. Five samples, unetched LFP/C, LFP/C treated with 0.5 M HCl for 8 min, 2 M HCl for 10 min and 4 h, and 12 M HCl for 8 h, are selected as the representative examples of various leaching stages (**Scheme 1B**).

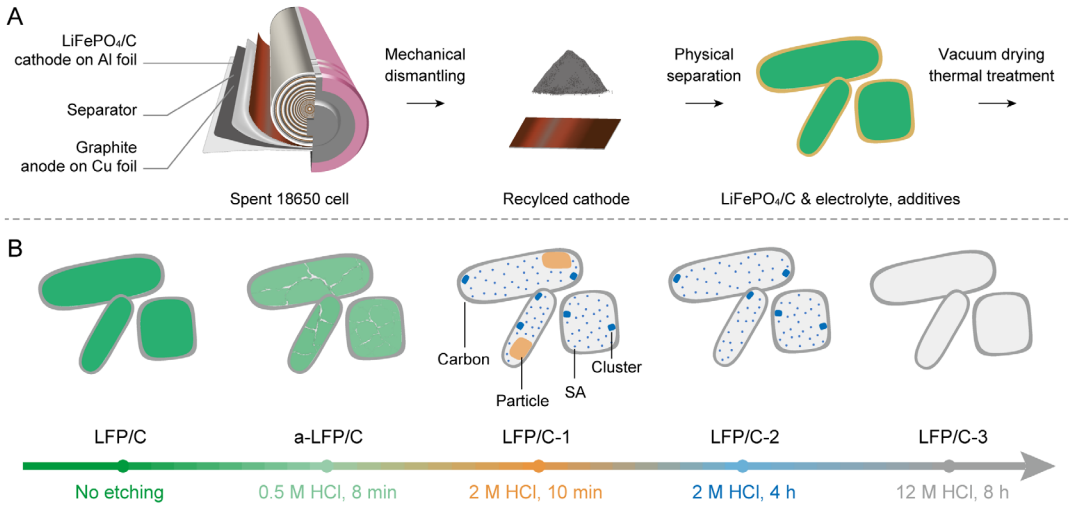

Scheme 1. (**A**) Upcycling process of spent 18650 $LiFePO_4$ LIB cell: mechanical dismantling, physical separation, post-thermal treatment, and partial etching. (**B**) Schematic illustration showing the partial etching process of the spent LFP/C cathode to a-LFP/C, LFP/C-1, LFP/C-2, and LFP/C-3. Etching conditions: HCl-to-sample ratio = 10 mL:1 mg, 25 °C (hot reflux at 100 °C for LFP-3).

The structural and morphologic evolution of LFP/C during the acid treatment was investigated by powder X-ray diffraction (XRD), scanning electron microscopy (SEM), and transmission electron microscopy (TEM). The pristine LFP/C exhibits a typical XRD pattern of triphylite phase (ICSD code: 260570, **Fig. 1A**),[27] confirming the presence of LFP as the only crystalline phase. SEM and TEM images in **Figs. S2a**, **S3a,** and **S4** reveal a core–shell structure with the ellipsoidal LFP particles wrapped by thin carbon layers (thickness = *ca.* 4 nm). A short (8 min) treatment of

LFP/C in 0.5 M HCl (a-LFP/C) leads to XRD peak broadening and reduced intensity, which is indicative of a decrease in structural ordering. Although a-LFP/C has a similar morphology as the pristine LFP/C (**Fig. S2b**), its TEM images (**Figs. S3b** and **S5**) show the amorphization of LFP particles. When treated with more concentrated HCl for longer periods (2 M HCl for 10 min and 4 h, LFP/C-1 and LFP/C-2), all XRD peaks disappear, suggesting the decomposition of the crystalline LFP core. A broad peak from the carbon matrix emerges at *ca.* 25°, corresponding to the graphite (002) plane. TEM images in **Fig. S3c** and **S3d** reveal hollow carbon shells of LFP/C-1 and LFP/C-2. In LFP/C-1, however, a few residual particles remain due to incomplete etching. Open cracks are apparent over the entire carbon shells of LFP/C-3 (**Fig. S2e**), suggesting the corrosion of the carbon sphere under harsh conditions (refluxing LFP/C in hot 12 M HCl for 8 h).[28]

The microstructure of LFP/C-1 was further probed by high-resolution TEM. **Figs. 1B** and **S6** unveil that the majority of the crystalline LFP is removed from LFP/C-1 with very few irregular particles encapsulated in carbon remaining.[29] The magnified image (**Fig. 1C**) and the corresponding fast Fourier transform (FFT) pattern (**Fig. 1D**) acquired on the [$1\bar{1}3$]-orientated crystal in LFP/C-1 show the (220) and (301) reflections of triphylite phase. **Figs. 1E** and **S6c** show the high-angle annular dark-field scanning transmission microscopic (HAADF-STEM) images and elemental mappings of two regions of LFP/C-1. Fe signal covers a much smaller area (d = *ca.* 20 nm) of the residual particle compared with P and O signals (d = *ca.* 50 nm), which contrasts with the pristine LFP particles that display similar areas for Li, Fe, P, and O elements. The removal of Fe atoms from the initial LFP structure may result from the weaker M–O bond than the covalent P–O bond.[30] Meanwhile, no signal is detected from Li because of its light atomic mass and low content. Considering its high reactivity, the majority of Li atoms are likely to be etched away by

HCl from LiO_6 octahedra of the olivine structure, accompanied by slower dissolution of FeO_6 octahedra and PO_4 tetrahedra.[31, 32]. The acid leaching and the subsequent air-drying convert the LFP to $FePO_4$ of a similar orthorhombic structure (*Pnma* space group, **Fig. S7**).[26]

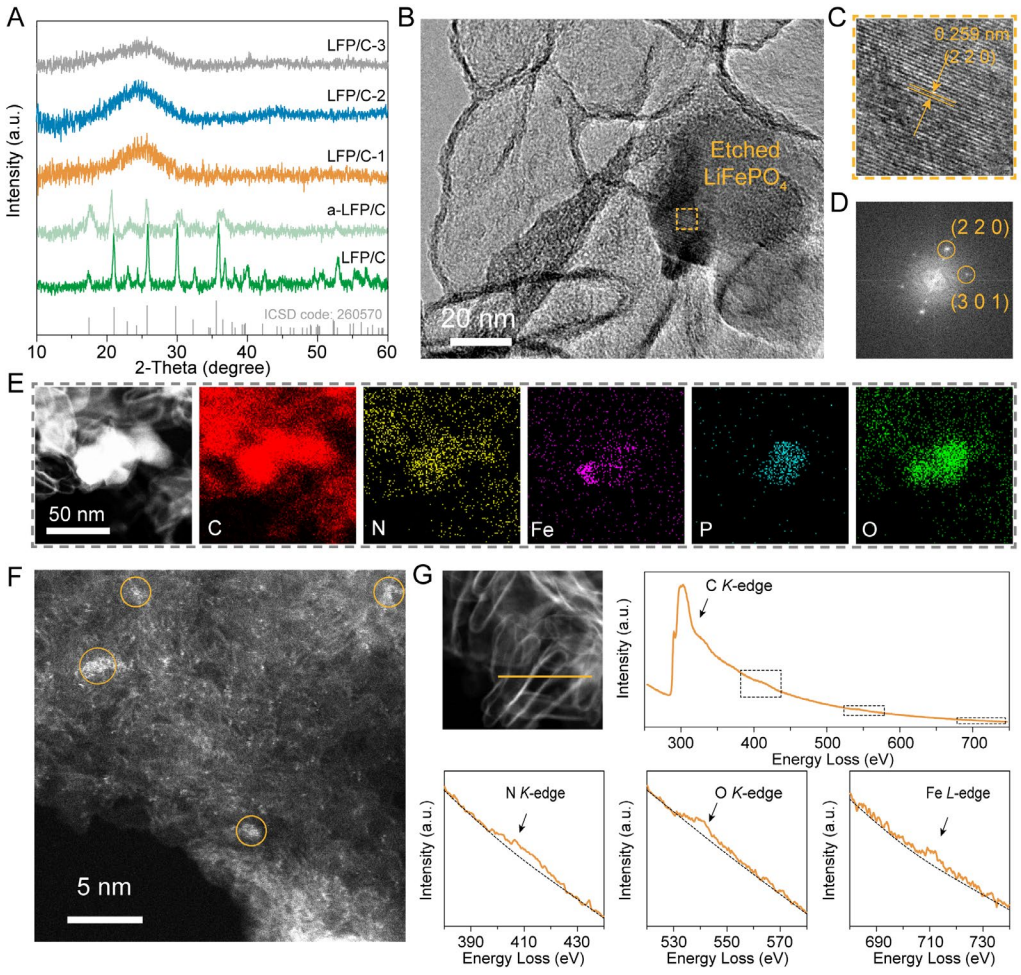

Figure 1. (**A**) Powder XRD patterns of LFP/C, a-LFP/C, LFP/C-1, LFP/C-2, and LFP/C-3. (**B**) TEM image of LFP/C-1. (**C**) A magnified TEM image showing the lattice planes of the etched LFP particle in LFP/C-1, (**D**) the corresponding FFT pattern, (**E**) HAADF-STEM and the corresponding EDX elemental mapping images, and (**F**) aberration-corrected HAADF-STEM image. (**G**) Typical EELS line scan across the hollow carbon sphere of LFP/C-1 and the corresponding HAADF image.

The decomposition of LFP particles is incomplete under mild etching conditions. We speculated that species other than the residual $FePO_4$ species may persist in the carbon shell of

LFP/C-1.[29] Aberration-corrected HAADF-STEM images of LFP/C-1 (**Figs. 1F** and **S8**) reveal that most Fe sites appear as isolated bright dots, most likely to be single atoms (SA_{Fe}), that are embedded in the carbon shell. In addition, several aggregated dots (yellow circles; d < 2 nm) are identified, suggesting the co-existence of Fe-containing clusters. The chemical composition of LFP/C-1 was further analyzed by electron energy-loss spectroscopy (EELS, **Fig. 1G**). The line scanning profiles recorded across a hollow carbon sphere displays the main peak at *ca.* 300 eV and a minor loss peak at *ca.* 410 eV, which correspond to C and N K-edges, respectively. The presence of O and Fe atoms is confirmed by two minor loss peaks at *ca.* 540 and 710 eV. These electron microscopic and spectroscopic results suggest that the isolated Fe atoms observed in **Fig. 1F** are bonded with O atoms in the surroundings and are further in contact with the N-doped carbon matrix. The presence of FeO_x clusters is also confirmed. The Fe–N coordination could be excluded because: 1) all the Fe species originate from the FeO_6 octahedron; and 2) breaking the Fe–O bond and forming a new Fe–N bond is not feasible under the mild reaction conditions engaged.

On the contrary, both LFP/C-2 and LFP/C-3 exhibit a morphology of hollow carbon spheres without any visible metal particles (**Figs. S9** and **S10**). Although less than those in LFP/C-1, several SAs and clusters are identified from the HAADF-STEM images of LFP/C-2 (**Fig. S8c** and **S8d**). Inductively coupled plasma optical emission spectrometry (ICP-OES, **Table S1**) and elemental analysis (**Table S2**) were conducted to qualitatively determine the compositional differences among LFP/C-1, LFP/C-2, and LFP/C-3. Notably, the total Fe loading amount in LFP/C-1 is 3.71 wt.%. A trace amount of Fe species (2.63 wt.%) still exists in LFP/C-2, while almost no Fe remains in LFP/C-3. The acid treatment of LFP/C samples creates voids in the carbon sphere, as evidenced by the N_2 adsorption–desorption isotherms and pore distribution plots in **Fig. S11**.

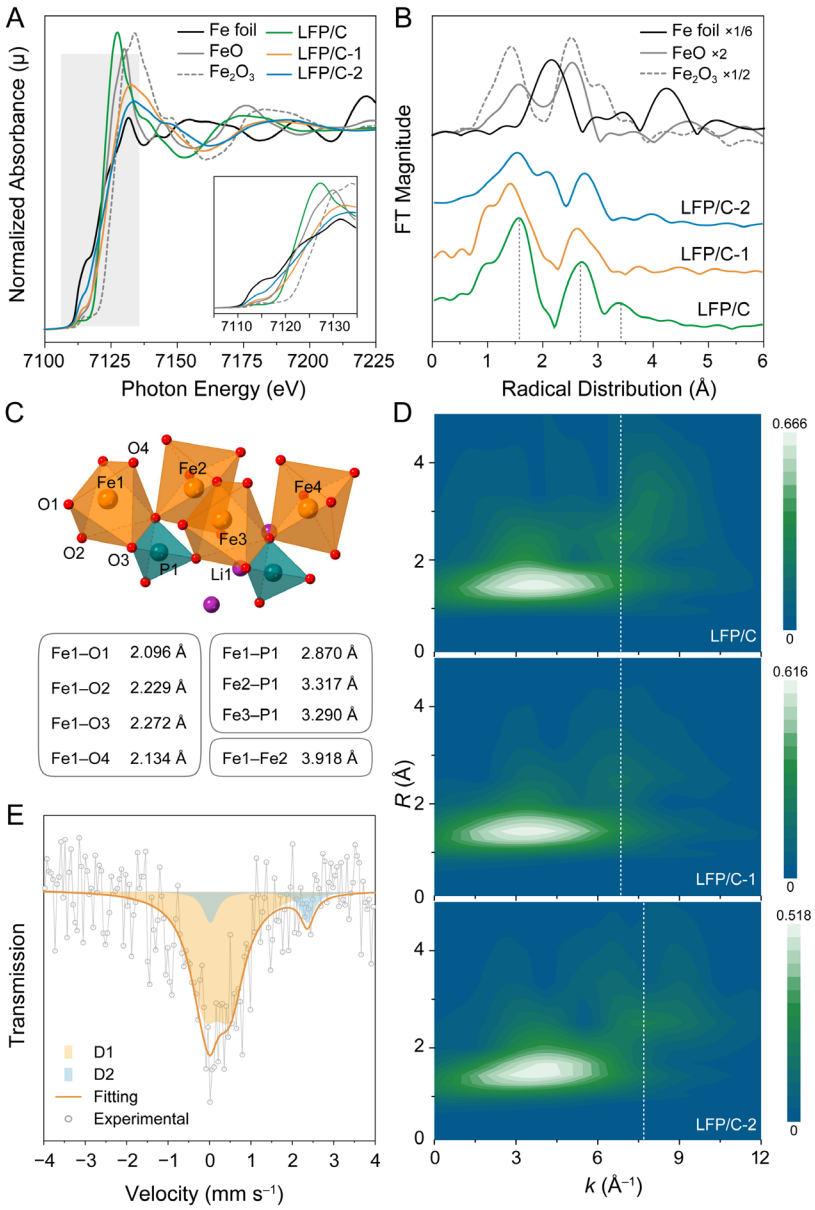

Figure 2. (**A** and **B**) Normalized Fe *K*-edge XANES spectra (**A**) and FT profiles of Fe *K*-edge k^2-weighted EXAFS data (**B**) of LFP/C, LFP/C-1, LFP/C-2, and reference samples of Fe foil, FeO and Fe_2O_3. (**C**) Calculated Fe–X (X = O, P, Fe) distances in $LiFePO_4$ olivine structure. (**D**) WT contour plots for EXAFS signals of LFP/C, LFP/C-1, and LFP/C-2. White dotted lines indicate the *k*-value shifting of Fe–P(Fe) scatterings at the high *k* range. (**E**) Mössbauer spectrum of LFP/C-1.

X-ray absorption spectroscopy (XAS) was employed to further investigate the electronic structure and local coordination environment of Fe species. **Fig. 2A** shows the Fe *K*-edge X-ray

absorption near edge structure (XANES) of pristine LFP/C, LFP/C-1, LFP/C-2, Fe foil, FeO and Fe_2O_3 reference. One weak pre-edge peak at *ca*. 7,112 eV in LFP/C corresponds to the dipole-forbidden $1s \rightarrow 3d$ transition for the octahedrally coordinated Fe sites. Besides, the $1s \rightarrow 4p$ and continuum transitions occur at *ca*. 7,118 eV.[33] The features of characteristic pre-edge peak and main absorption edge are similar for FeO and octahedral O-coordinated Fe(II) compounds (FeC_2O_4 and $[Fe(H_2O)_6][SiF_6]$),[34] indicating that the average Fe oxidation state is +2 in LFP/C. For LFP/C-1 and LFP/C-2, their pre-edge peaks are more intense and, together with the absorption edges, are shifted toward higher energies, similar to those of Fe_2O_3 and delithiated $FePO_4$.[34] This suggests that the valence states of Fe in LFP/C-1 and LFP/C-2 are mainly +3.

The corresponding Fourier transformed (FT) profiles of the k^2-weighted $\chi(k)$ function of extended X-ray absorption fine structure (EXAFS, without phase correction) are shown in **Fig. 2B**. The results were further fitted to investigate the coordination environments of Fe species (**Fig. S12** and **Table S3**). Various radial distances between Fe and X (X = O, P, Fe, and Li) are obtained from the LFP crystal structure (**Fig. 2C**), offering the crystallographic basis for analyzing the scattering contribution of different atomic shells around X-ray absorbing Fe atoms. The pristine LFP/C displays the main peak at *ca*. 2.07 Å (after phase correction, the same below), which corresponds to the first shell of Fe–O coordination in the distorted FeO_6 octahedra. The second dominant signal is assigned to the scatterings between Fe and adjacent P atoms (*ca*. 2.89 and 3.30 Å) corresponding to the values of Fe1–P1 and Fe2–P1 shown in **Fig. 2C**. Besides, a relatively weak peak (*ca.* 3.90 Å) arises from the long-range Fe–Fe path from the adjacent FeO_6 octahedrons. The fitted coordination numbers of Fe–O, Fe–P, Fe–P, and Fe–Fe in LFP/C are 4.33, 1.15, 1.02, and 0.74, respectively.[34]

For LFP/C-2, the first predominant peak is better fitted by two Fe–O paths at 2.09 and 2.22 Å (**Fig. 2B**), suggesting a relatively disordered environment of Fe as compared to that of LFP. Nevertheless, the fitted result is consistent with the results of electron microscopic analyses, suggesting that the isolated Fe sites (SA_{Fe}) with coordination to the surrounding O atoms are the major Fe species and FeO_x clusters are the minor species in this sample. The interatomic distance for the third neighboring shell of Fe is *ca.* 3.01 Å, a value relatively close to the corresponding values of Fe-P for LFP (2.89 and 3.30 Å). However, it can not be unambiguously assigned to Fe-P coordination because of the possible contribution of Fe–Fe scattering in the FeO_x clusters in LFP/C-2. Wavelet transform (WT) analysis was further conducted to combine the insights into *k*- and *R*-space resolutions. As shown in **Fig. 2D**, the peak of LFP/C-2 at a high *k* value (*ca*. 7.8 $Å^{-1}$) displays an obvious positive shift compared with that of LFP/C (*ca*. 6.8 $Å^{-1}$). This suggests that the third shell signal does not attribute to Fe–P but rather to heavier Fe–Fe scattering in FeO_x clusters.

For LFP/C-1, the existence of various types of Fe species complicates its EXAFS analysis, and only averaged coordination information could be provided. The FT profile of LFP/C-1 displays prevailing peaks at *ca.* 1.97, 2.83, 3.31, and 3.99 Å, which may be reasonably assigned to the Fe–O, Fe–P, Fe–P, and Fe–Fe shells of the residual $FePO_4$ in this sample, respectively. These peaks are relatively weak in intensity, and the fitted values of coordination numbers are much smaller (4.75, 0.61, 0.90, and 0.32) than the corresponding values for the pristine LFP/C. The contributions from possibly existing SA_{Fe} and FeO_x clusters should be even weaker and are believed to overlap with those of $FePO_4$.

The Fe species in LFP/C-1 was further analyzed using Mössbauer spectroscopy (**Fig. 2E** and **Table S4**). The doublet D1 in the deconvoluted spectrum indicates the isomer shift (IS) and

quadrupole splitting (QS) of 0.19 and 0.62 mm s^{-1}, respectively. This can be assigned to the Fe^{3+} single sites coordinated to O (87.5 area%).[35] A weaker doublet D2 represents 12.5 % of the resonance area and is attributed to olivine-type FeO_6 with the IS and QS of 1.20 and 2.34 mm s^{-1}, respectively.[26, 36] Overall, the results confirm the co-existence of SA and non-SA Fe species. Further differentiation and quantification of clusters or particles are not possible due to the limitation of spectroscopic resolution and the similarity of Fe species in FeO_6 and $FePO_4$.

The etched LFP/C samples containing the Fe species stabilized in carbon spheres are believed to possess excellent oxygen electroreduction activity. Using a standard three-electrode cell, the electrocatalytic performances of the LFP/C catalysts and commercial Pt/C (20 wt.%) were evaluated under alkaline conditions (high purity 1 M KOH). **Fig. S13a** compares the cyclic voltammograms (CV) collected on a rotating disk electrode (RDE) in O_2- and Ar-saturated electrolytes, and the onset potentials (E_{onset}) and half-wave potentials ($E_{1/2}$) are summarized in **Fig. S13b**. The pristine LFP/C records the lowest ORR performance with an E_{onset} of merely 0.79 V *vs.* reversible hydrogen electrode (RHE), most probably due to the limited active metal sites exposed for the catalytic reaction. LFP/C-1 affords a very high E_{onset} of 0.97 V, which is close to that of Pt/C (0.99 V), while LFP/C-2 and LFP/C-3 display lower E_{onset} values of 0.92 and 0.83 V, respectively. In linear sweep voltammetry (LSV, **Fig. 3A**), LFP/C-1 exhibits a superior ORR activity with $E_{1/2}$ of 0.89 V, outperforming Pt/C (0.88 V), LFP/C-2 (0.85 V), LFP/C-3 (0.82 V), and LFP/C (0.72 V). The Tafel plots (**Fig. S13c**) obtained from the polarization curves verify such differences in the kinetic behaviors of the samples. LFP/C-1 yields the lowest Tafel slope of 61.0 mV dec^{-1}, followed by LFP/C-3 (70.5 mV dec^{-1}), LFP/C-2 (71.4 mV dec^{-1}), LFP/C (85.4 mV dec^{-1}), and Pt/C (113.1 mV dec^{-1}), which confirms the fastest kinetic process of LFP/C-1 among all samples studied.

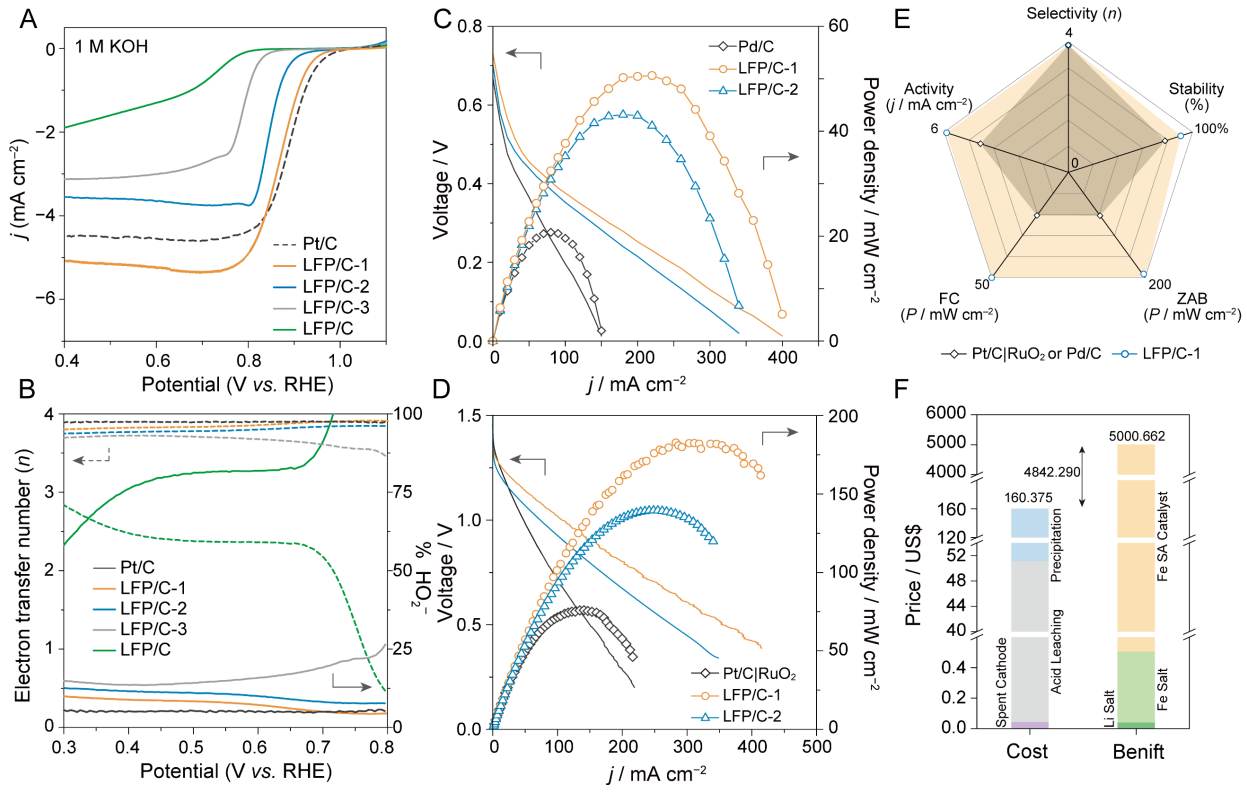

Figure 3. (**A**) ORR polarization curves at 1,600 rpm in O_2-saturated 1 M KOH. (**B**) Electron transfer number (*n*) and HO_2^- yield plotted against applied potential. (**C**) Discharge polarization curves of FCs constructed with LFP/C-1, LFP/C-2, and Pd/C and the corresponding power density plots. (**D**) Discharge polarization curves and the corresponding power density plots of rechargeable ZABs constructed with LFP/C-1 and Pt/C+RuO_2. (**E**) Radar chart summarizing ORR activity, selectivity, stability, and the corresponding power densities of the FC and ZAB. (**F**) Total cost and benifit of treating 1 kg of spent LFP/C cathode materials.

The K–L plots given in **Fig. S14** display good linear relationships between the reciprocal current and reciprocal square root of rotating speed for all catalysts, indicating their first-order reaction process. **Fig. 3B** compares the calculated electron transfer number (*n*) and peroxide yield (% HO_2^-) derived from the polarization curves (**Fig. S15**). LPF/C-1 demonstrates a large *n* value (> 3.8) and a very low % HO_2^- (< 10 %) in the potential window between 0.3 and 0.8 V, which is comparable to that of Pt/C. These results confirm the superior selectivity of LFP/C-1 for the four-

electron oxygen reduction path. The durability of catalysts was assessed by chronoamperometric response and cycling aging tests (**Fig. S16**). LFP/C-1 demonstrates good stability in a 16-h test, retaining 90.5 % of the initial current density, which is much better than Pt/C (77.9 %). The $E_{1/2}$ and diffusion-limited current density of LFP/C-1 shows only slight declines of 6 mV and 0.3 mA cm^{-2}, respectively, after continuous 500 cycles, which is consistent with X-ray photoelectron spectroscopic (XPS) and TEM analyses before and after cycling (**Figs. S17**−**S19**). Moreover, unlike Pt/C, LFP/C-1 exhibits a great tolerance to methanol crossover (inset in **Fig. S16**).

The performances of the ammonia fuel cell (FC) and rechargeable Zn–air battery (ZAB) engaging the etched LFP/C samples were evaluated (**Figs. S20)**. **Fig. 3C** shows the operation of a FC made of LFP/C samples as both anode and cathode using ammonia as the fuel at 80 °C. The current densities of LFP/C-1, LFP/C-2, and commercial Pd/C are measured as *ca.* 240, 203, and 100 mA cm^{-2} at 0.20 V, respectively. LFP/C-1 delivers the highest maximum power density of 51 mW cm^{-2} at 0.26 V, largely exceeding that of Pd/C (21 mW cm^{-2} at 0.20 V) and LFP/C-2 (43 mW cm^{-2} at 0.24 V). In a constant *i*-t test with a current density of 20 mA cm^{-2} at 80 °C as the challenging condition for durability evaluation (**Fig. S21**), the cell voltage of the LFP/C-1-based FC shows a slow decay over a period of 6 h. The ZAB fabricated with LFP/C-1 displays the highest discharging current density of *ca.* 410 mA cm^{-2} under a high voltage (**Fig. 3D**). Its peak power density (*ca.* 185 mW cm^{-2}) surpasses that of LFP/C-2 (*ca.* 123 mW cm^{-2}) and Pt/C+RuO_2 (*ca.* 76 mW cm^{-2}). LFP/C-1 achieves a stable potential at all currents with good reversibility as demonstrated by well-retained working voltage after high-rate charge/discharge (10, 20, and 50 mA cm^{-2}, **Fig. S22a**). **Fig. S22b** compares their long-term durability test results where the ZABs are cycled for 240 h (120 cycles) at high current densities. The cycling performance of LFP/C-1 is superior to Pt/C+RuO_2 as reflected by a slight increase in charge/discharge voltage gap (58 mV),

compared with 108 mV in Pt/C+RuO_2. The Radar chart in **Fig. 3E** summarizes the half-cell reaction and the practical device performances from five dimensions (ORR activity, selectivity, stability, and power densities of FC and ZAB), which illustrates the superior behaviors of LFP/C-1 over commercial catalysts and proves the potential of secondary utilization of waste LIB cathode. As summarized in **Table S5**, the performances of LFP/C-1 in ammonia FC and ZAB are comparable, if not better, to other recently reported Fe-based electrocatalysts. Lastly, a simple economic assessment was conducted to evaluate the advantages of constructing such atomic-scale catalysts (**Fig. 3F** and **Table S6**).[37] Based on the estimated costs (US$ 160.37 per kg) of spent LFP/C cathode, acid leaching, and precipitation of metal species, the profit of producing active SA_{Fe}-based ORR catalyst is calculated as US$ 4,842.29 per kg, which demonstrates that the proposed upcycling process is economically feasible.

The only active site in LFP/C-3 is N-doped carbon possessing low ORR activity, which explains its poor ORR performance. However, is the performance difference between LFP/C-1 and LFP/C-2 only due to the different composition of Fe species? According to our previous findings,[20] metallic Fe nanoclusters own a very poor intrinsic ORR activity but can alter the binding strengths of intermediates on the adjacent Fe–N_4 SA site, therefore optimizing the ORR energy barriers. In this work, the roles of the residual $FePO_4$ particles and FeO_x nanoclusters in the vicinity of O-coordinated SA_{Fe} sites are still ambiguous.

To exclude the contribution from low-active species and comprehend the effects of the local environment of SA_{Fe} on ORR performance, poisoning experiments were carried out by adding 10 mM SCN^- into 0.5 M H_2SO_4 (**Fig. 4A**).[38, 39] As expected, the addition of SCN^- causes no decline in the ORR activity of LFP/C-3 that contains no SA_{Fe} sites. On the contrary, the ORR performances of LFP/C-2 and LFP/C-1 are notably suppressed, which indicates the existence of SA_{Fe} sites in

both samples. In particular, after the complete inhibition of SA_{Fe} sites, the $E_{1/2}$ of LFP/C-1 and LFP/C-2 are reduced by 40 mV and 15 mV, respectively, to almost the same value of LFP/C-3 (0.445 V), which is mostly composed of carbon. This phenomenon suggests that (1) SA_{Fe} contributes the most to ORR activities of LFP/C-1 and LFP/C-2, and (2) the direct contribution from non-SA species, namely, nanoscale $FePO_4$ residues and FeO_x clusters, is much lower. The difference in ORR activities of LFP/C-1 and LFP/C-2 seems to mainly arise from their distinctive neighboring non-SA species that modulate the property of the SA_{Fe} site.

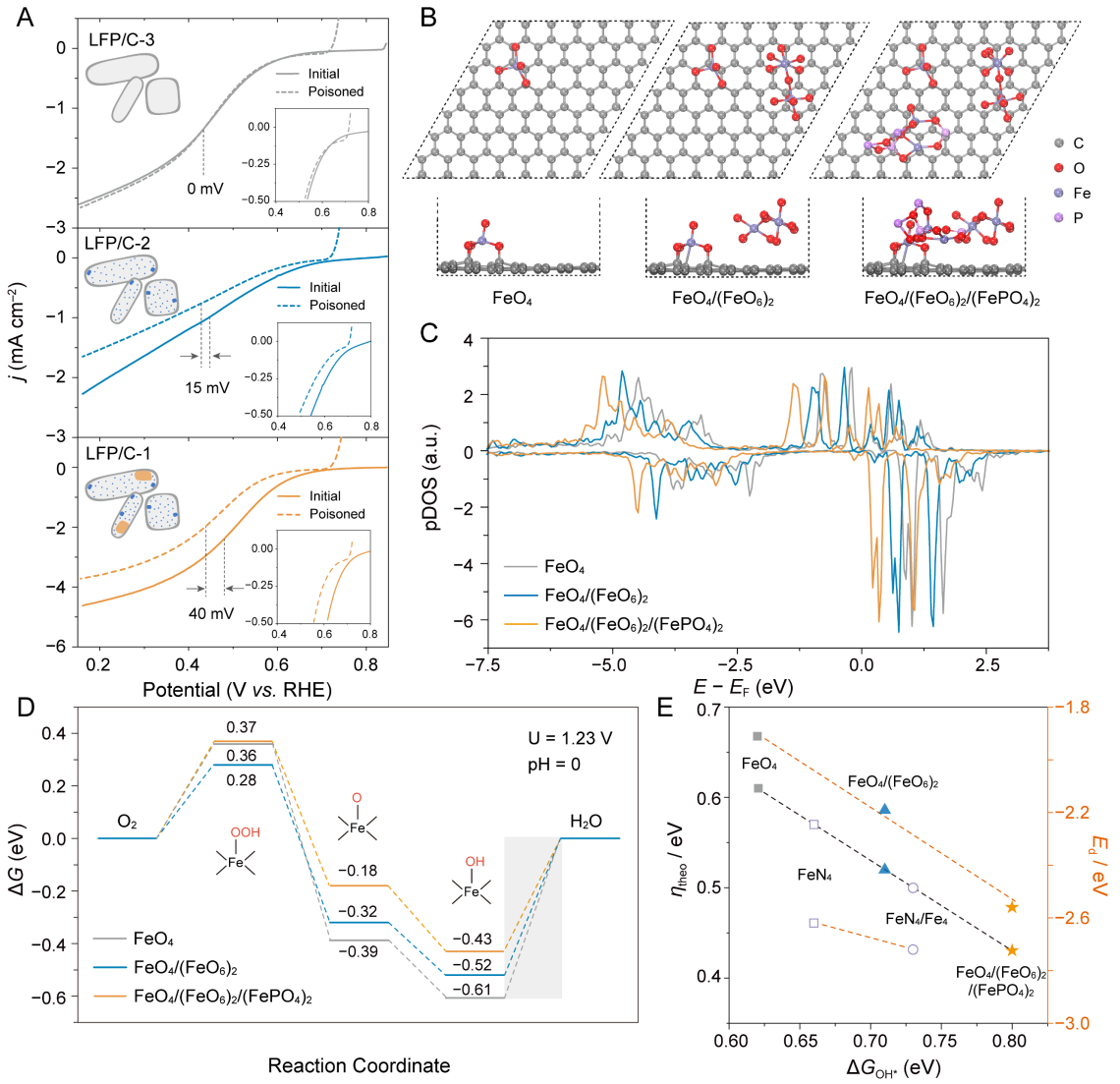

Figure 4. (**A**) SCN^- poisoning experiments represented by LSV curves in 0.5 M H_2SO_4. (**B**) Top-views and side-views of modeling structures of FeO_4, $FeO_4/(FeO_6)_2$, and $FeO_4/(FeO_6)_2/(FePO_4)_2$ on graphene slabs. (**C**) Projected density of states for the corresponding models. (**D**) The corresponding free energy diagrams for ORR at U = 1.23 V, pH = 0. (**E**) Linear relationships of the theoretical overpotential (η_{theo}) and *d*-band center energy value (E_d) with the Gibbs free energy of OH* (ΔG_{OH*}).

Further insight into the synergistic effect among the different Fe sites was obtained through first-principles calculations. With the consideration of the structure of pristine LFP/C (LFP crystal encapsulated by carbon shell *via* C–O coordination) and the microscopic and spectroscopic evidences (*e.g.*, coordination number and cluster size), graphene slab models containing surface attached unsaturated FeO_4, $(FeO_6)_2$ cluster, and/or $(FePO_4)_2$ bulk unit cell were constructed to analyze the possible synergies among the neighbors (**Fig. 4B**). Both the $(FeO_6)_2$ cluster and $(FePO_4)_2$ display inferior activities due to the strong bindings of O* and high energy barriers, FeO_4 is believed to be the main active center in each structure. Bader charge analysis manifests that the multiple metal species function as a "charge modulator", pulling electrons thereby altering the net charge of Fe in FeO_4, with the values of 1.49|e|, 1.50|e|, and 1.52|e| for FeO_4, $FeO_4/(FeO_6)_2$, and $FeO_4/(FeO_6)_2/(FePO_4)_2$, respectively. As a result, the projected density of the states (PDOS) of the Fe *d* orbitals in FeO_4 for the three models demonstrates that their *d*-band center energy (E_d) relative to the Fermi level (E_F) gradually decreases with the incorporation of the $(FeO_6)_2$ cluster and $(FePO_4)_2$ (**Fig. 4C**). Such electron pulling behaviors can modulate the electronic configuration of FeO_4, which causes more electronic occupancy in the antibonding states, therefore weakening the corresponding adsorption.[40]

Figs. S23 and **4D** display the ORR pathways and energetic profiles on the FeO_4 site, respectively, which consists of four elementary electron/proton-coupled steps. In general, the rate-determining step for FeO_4, $FeO_4/(FeO_6)_2$, and $FeO_4/(FeO_6)_2/(FePO_4)_2$ is the oxygen protonation of

OH*, with the limiting energy barriers of 0.61, 0.52, and 0.43 eV, respectively. The introduction of $(FeO_6)_2/(FePO_4)_2$ is suggested to induce the weaker chemical binding with intermediates on the FeO_4 site, directly leading to enhanced ORR activity. Considering similar systems that have been previously reported[41, 42] and our previous work on FeN_4 SA and adjacent Fe_4 cluster,[20] we correlate their E_d and theoretical overpotentials (η_{theo}) with the Gibbs free energy of OH* (ΔG_{OH*}) as shown in **Fig. 4E** and **Tables S7**−**S8**. The constructed linear plots indicate that the presence of nearby $(FeO_6)_2/(FePO_4)_2$ endows the FeO_4 site with the optimum *d*-state level, demonstrating the universality of this strategy to modulate the SA ORR activity by introducing proper cluster/particle-type neighbors. Overall, these calculation results manifest the preference of adjacent multi-atomic species for stimulating the intrinsic activity of FeO_4, although these multi-atomic species do not directly contribute much to the ORR catalytic process.

Unlike most reported SA sites that are coordinated with N atoms (*e.g.*, $Fe–N_4$), the mild reaction conditions do not form Fe–N bonds in our LFP/C samples. It is interesting to know whether the $(FeO_6)_2/(FePO_4)_2$ nearby the SA_{Fe} sites of different coordination would have the same effect on their ORR activities. To demonstrate the effect of SA-coordination atom, three similar models, but with the replacement of all surface-attached $Fe–O_4$ sites by planar $Fe–N_4$ embedded in a graphene slab, were established (**Fig. S25a**). It turns out that the low *d*-band center of $Fe–N_4$ (E_d = −2.62 eV) is greatly upshifted when accompanied by $(FeO_6)_2$ or $(FeO_6)_2/(FePO_4)_2$ (**Fig. S25b**). This leads to the significant changes in energy barriers of each elementary step (**Fig. S25c**), and finally drags down the catalytic activity of $Fe–N_4$ itself, as manifested by the overpotential trend of FeN_4 (0.57 eV) < $FeN_4/(FeO_6)_2$ (0.61 eV) < $FeN_4/(FeO_6)_2/(FePO_4)_2$ (0.66 eV). Overall, although the introduction of foreign cluster/particle to affect the intrinsic catalytic activity of SA is a general strategy, the selection of the right coordination is critical for higher performance. The

reason for the shifted *d*-band of the catalytic site needs to be further explored with more accurate models that can simulate the real catalyst structure, and the model library to elucidate the interaction between sites needs to be further established.

To conclude, we report a case study of upcycling end-of-life $LiFePO_4$ cathode materials *via* a facile partial etching strategy. O-coordinated SA_{Fe} sites were created inside the hollow N-doped carbon spheres with a few nanoscale FeO_x clusters and $FePO_4$ nanoparticles. The resultant material exhibits excellent ORR activity/stability in an alkaline medium as manifested by the high E_{onset} of 0.97 V and the slight current decline of 9.5 % after a 16-h test. It also displays promising potential in practical ammonia FC and ZAB. The etching strategy breaks a long-standing stereotype by innovatively constructing atomic catalytic sites *via* a top-down approach. More importantly, this work demonstrates the potential value of spent LIB electrodes in the half-cell reaction of FC and ZAB and builds a bridge between energy storage and conversion systems by a facile upcycling approach.

ASSOCIATED CONTENT

Supporting Information.

Experimental details of physical characterizations, electrochemical measurements, Zn-air battery test, ammonia fuel cell test, and computational methods; flow charts of LFP/C upcycling routes; SEM, TEM, and AC-HAADF-STEM images of etched samples; schematic diagrams of LFP crystal structure; BET analysis; XPS analysis; EXAFS analysis; electrochemical ORR measurements including CV, LSV, Tafel plot, K−L plot, amperometry test; ammonia fuel cell and

Zn−air battery test; theoretical model for DFT calculations, reaction free energy diagram, and PDOS.

AUTHOR INFORMATION

Corresponding Authors

Chia-Min Yang − Department of Chemistry, National Tsing Hua University, Hsinchu 300034, Taiwan; Frontier Research Center on Fundamental and Applied Sciences of Matters, National Tsing Hua University, Hsinchu 300034, Taiwan; orcid.org/0000-0001-9990-4779; Email: cmyang@mx.nthu.edu.tw

Lawrence Yoon Suk Lee − Department of Applied Biology and Chemical Technology and the State Key Laboratory of Chemical Biology and Drug Discovery, The Hong Kong Polytechnic University, Kowloon, Hong Kong, SAR, China; Research Institute for Smart Energy, The Hong Kong Polytechnic University, Kowloon, Hong Kong, SAR, China; orcid.org/0000-0002-6119-4780; Email: lawrence.ys.lee@polyu.edu.hk

Authors

Mengjie Liu − Department of Applied Biology and Chemical Technology and the State Key Laboratory of Chemical Biology and Drug Discovery, The Hong Kong Polytechnic University, Kowloon, Hong Kong, SAR, China

Tsung-Cheng Yang − Department of Chemistry, National Tsing Hua University, Hsinchu 300034, Taiwan

Zhefei Pan − Department of Mechanical Engineering, The Hong Kong Polytechnic University, Hung Hom, Kowloon, Hong Kong SAR, China

Jeongyeon Lee − Department of Applied Biology and Chemical Technology and Research Institute for Smart Energy, The Hong Kong Polytechnic University, Hung Hom, Kowloon, Hong Kong SAR, China

Liang An − Department of Mechanical Eng[43]ineering, The Hong Kong Polytechnic University, Hung Hom, Kowloon, Hong Kong SAR, China

Baolong Qiu − Key Laboratory for Ecological Metallurgy of Multimetallic Mineral of Ministry of Education, School of Metallurgy, Northeastern University, Shenyang, 110819, P. R. China

Huayi Yin − Key Laboratory for Ecological Metallurgy of Multimetallic Mineral of Ministry of Education, School of Metallurgy, Northeastern University, Shenyang, 110819, P. R. China and School of Resource and Environmental Science, Wuhan University, Wuhan, 430072, P. R. China

Notes

The authors declare no competing financial interest.

ACKNOWLEDGMENT

M.J. Liu and T-C. Yang contributed equally to this study. The authors gratefully acknowledge the financial supports from the Research Grants Council of the Hong Kong SAR, China (PolyU15217521), the Hong Kong Polytechnic University (Q-CDA3), the Environmental Protection Department of the Hong Kong SAR, China (GTF202020051), Shenzhen Key Basic Research Project, China (JCYJ20220818102210023), the Ministry of Science and Technology, Taiwan (MOST 109-2113-M-007-018-MY3 and MOST 109-2634-F-007-023). National

Synchrotron Radiation Research Centre, Taiwan is gratefully acknowledged for XAS characterizations.

REFERENCES

(1) H. Kawamura, M. L., K. Iversen, H. W. J. Cheng. *Frontier Technology Issues: Lithium-Ion Batteries: A Pillar for a Fossil Fuel-Free Eeconomy?* 2022. https://www.un.org/development/desa/dpad/publication/frontier-technology-issues-lithium-ion-batteries-a-pillar-for-a-fossil-fuel-free-economy/ (accessed in November 2022).

(2) Liu, K.; Liu, Y.; Lin, D.; Pei, A.; Cui, Y. Materials for Lithium-Ion Battery Safety. *Sci. Adv.* **2018**, *4* (6), 9820-9830.

(3) Zhang, X.; Li, L.; Fan, E.; Xue, Q.; Bian, Y.; Wu, F.; Chen, R. Toward Sustainable and Systematic Recycling of Spent Rechargeable Batteries. *Chem. Soc. Rev.* **2018**, *47* (19), 7239-7302.

(4) Ahmadi, L.; Young, S. B.; Fowler, M.; Fraser, R. A.; Achachlouei, M. A. A Cascaded Life Cycle: Reuse of Electric Vehicle Lithium-Ion Battery Packs in Energy Storage Systems. *Int. J. Life Cycle Assess.* **2017**, *22* (1), 111-124.

(5) Baum, Z. J.; Bird, R. E.; Yu, X.; Ma, J. Lithium-Ion Battery Recycling—Overview of Techniques and Trends. *ACS Energy Lett.* **2022**, *7* (2), 712-719.

(6) Natarajan, S.; Aravindan, V. Burgeoning Prospects of Spent Lithium-Ion Batteries in Multifarious Applications. *Adv. Energy Mater.* **2018**, *8* (33), 1802303.

(7) Larcher, D.; Tarascon, J. M. Towards Greener and More Sustainable Batteries for Electrical Energy Storage. *Nat. Chem.* **2015**, *7* (1), 19-29.

(8) Harper, G.; Sommerville, R.; Kendrick, E.; Driscoll, L.; Slater, P.; Stolkin, R.; Walton, A.; Christensen, P.; Heidrich, O.; Lambert, S.; Abbott, A.; Ryder, K.; Gaines, L.; Anderson, P. Recycling Lithium-Iion Batteries from Electric Vehicles. *Nature* **2019**, *575* (7781), 75-86.

(9) Sun, W.; Wang, F.; Zhang, B.; Zhang, M.; Küpers, V.; Ji, X.; Theile, C.; Bieker, P.; Xu, K.; Wang, C.; Winter, M. A Rechargeable Zinc-Air Battery Based on Zinc Peroxide Chemistry. *Science* **2021**, *371* (6524), 46-51.

(10) Li, Y.; Dai, H. Recent Advances in Zinc–Air Batteries. *Chem. Soc. Rev.* **2014**, *43* (15), 5257-5275.

(11) Steele, B. C. H.; Heinzel, A. Materials for Fuel-Cell Technologies. *Nature* **2001**, *414* (6861), 345-352.

(12) Li, Z.; Wang, W.; Qian, Q.; Zhu, Y.; Feng, Y.; Zhang, Y.; Zhang, H.; Cheng, M.; Zhang, G. Magic Hybrid Structure as Multifunctional Electrocatalyst Surpassing Benchmark Pt/C Enables Practical Hhydrazine Fuel Cell Integrated with Energy-Saving H_2 Production. *eScience* **2022**, *2* (4), 416-427.

(13) Yang, Y.; Zhong, Y.; Shi, Q.; Wang, Z.; Sun, K.; Wang, H. Electrocatalysis in Lithium Sulfur Batteries under Lean Eelectrolyte Conditions. *Angew. Chem.* **2018**, *57* (47), 15549-15552.

(14) Wang, P.; Xi, B.; Huang, M.; Chen, W.; Feng, J.; Xiong, S. Emerging Catalysts to Promote Kinetics of Lithium–Sulfur Batteries. *Adv. Energy Mater.* **2021**, *11* (7), 2002893.

(15) Zhang, B.-W.; Sheng, T.; Liu, Y.-D.; Wang, Y.-X.; Zhang, L.; Lai, W.-H.; Wang, L.; Yang, J.; Gu, Q.-F.; Chou, S.-L.; Liu, H.-K.; Dou, S.-X. Atomic Cobalt as an Efficient Electrocatalyst in Sulfur Cathodes for Superior Room-Temperature Sodium-Sulfur Batteries. *Nat. Commun,* **2018**, *9* (1), 4082.

(16) Stamenkovic, V. R.; Strmcnik, D.; Lopes, P. P.; Markovic, N. M. Energy and Fuels from Electrochemical Interfaces. *Nat. Mater.* **2017**, *16* (1), 57-69.

(17) Wang, X.; Li, Z.; Qu, Y.; Yuan, T.; Wang, W.; Wu, Y.; Li, Y. Review of Metal Catalysts for Oxygen Reduction Reaction: From Nanoscale Engineering to Atomic Design. *Chem* **2019**, *5* (6), 1486-1511.

(18) Liu, M.; Wang, L.; Zhao, K.; Shi, S.; Shao, Q.; Zhang, L.; Sun, X.; Zhao, Y.; Zhang, J. Atomically Dispersed Metal Catalysts for the Oxygen Reduction Reaction: Synthesis, Characterization, Reaction Mechanisms and Electrochemical Energy Applications. *Energy Environ. Sci.* **2019**, *12* (10), 2890-2923.

(19) Zhang, S.; Chen, M.; Zhao, X.; Cai, J.; Yan, W.; Yen, J. C.; Chen, S.; Yu, Y.; Zhang, J. Advanced Noncarbon Materials as Catalyst Supports and Non-Noble Electrocatalysts for Fuel Cells and Metal–Air Batteries. *Electrochem. Energy Rev.* **2021**, *4* (2), 336-381.

(20) Liu, M.; Lee, J.; Yang, T.-C.; Zheng, F.; Zhao, J.; Yang, C.-M.; Lee, L. Y. S. Synergies of Fe Single Atoms and Clusters on N-Doped Carbon Electrocatalyst for pH-Universal Oxygen Reduction. *Small Methods* **2021**, *5* (5), 2001165.

(21) Han, G.; Zhang, X.; Liu, W.; Zhang, Q.; Wang, Z.; Cheng, J.; Yao, T.; Gu, L.; Du, C.; Gao, Y.; Yin, G. Substrate Strain Tunes *Operando* Geometric Distortion and Oxygen Reduction Activity of CuN_2C_2 Aingle-Atom Sites. *Nat. Commun,* **2021**, *12* (1), 6335.

(22) Li, X.; Xiang, Z. Identifying the Impact of the Covalent-Bonded Carbon Matrix to FeN_4 Sites for Acidic Oxygen Reduction. *Nat. Commun,* **2022**, *13* (1), 57.

(23) Han, G.-F.; Li, F.; Rykov, A. I.; Im, Y.-K.; Yu, S.-Y.; Jeon, J.-P.; Kim, S.-J.; Zhou, W.; Ge, R.; Ao, Z.; Shin, T. J.; Wang, J.; Jeong, H. Y.; Baek, J.-B. Abrading Bulk Metal into Single Atoms. *Nat. Nanotech.* **2022**, *17*, 403–407.

(24) Yang, H.; Liu, Y.; Liu, X.; Wang, X.; Tian, H.; Waterhouse, G. I. N.; Kruger, P. E.; Telfer, S. G.; Ma, S. Large-Scale Synthesis of N-Doped Carbon Capsules Supporting Atomically Dispersed Iron for Efficient Oxygen Reduction Reaction Electrocatalysis. *eScience* **2022**, *2* (2), 227-234.

(25) Liu, L.; Corma, A. Confining Isolated Atoms and Clusters in Crystalline Porous Materials for Catalysis. *Nat. Rev. Mater.* **2021**, *6* (3), 244-263.

(26) Shin, E. J.; Kim, S.; Noh, J.-K.; Byun, D.; Chung, K. Y.; Kim, H.-S.; Cho, B.-W. A Green Recycling Process Designed for $LiFePO_4$ Cathode Materials for Li-Ion Batteries. *J. Mater. Chem. A* **2015**, *3* (21), 11493-11502.

(27) Paolella, A.; Faure, C.; Bertoni, G.; Marras, S.; Guerfi, A.; Darwiche, A.; Hovington, P.; Commarieu, B.; Wang, Z.; Prato, M.; Colombo, M.; Monaco, S.; Zhu, W.; Feng, Z.; Vijh, A.; George, C.; Demopoulos, G. P.; Armand, M.; Zaghib, K. Light-Assisted Delithiation of Lithium Iron Phosphate Nanocrystals towards Photo-Rechargeable Lithium Ion Batteries. *Nat. Commun,* **2017**, *8* (1), 14643.

(28) Chen, J. P.; Wu. Acid/Base-Treated Activated Carbons: Characterization of Functional Groups and Metal Adsorptive Properties. *Langmuir* **2004**, *20* (6), 2233-2242.

(29) Fan, L.; Liu, P. F.; Yan, X.; Gu, L.; Yang, Z. Z.; Yang, H. G.; Qiu, S.; Yao, X. Atomically Isolated Nickel Species Anchored on Graphitized Carbon for Efficient Hydrogen Evolution Electrocatalysis. *Nat. Commun,* **2016**, *7* (1), 10667.

(30) Wang, J.; Sun, X. Understanding and Recent Development of Carbon Coating on $LiFePO_4$ Cathode Materials for Lithium-Ion Batteries. *Energy Environ. Sci.* **2012**, *5* (1), 5163-5185.

(31) Castro, L.; Dedryvère, R.; El Khalifi, M.; Lippens, P. E.; Bréger, J.; Tessier, C.; Gonbeau, D. The Spin-Polarized Electronic Structure of $LiFePO_4$ and $FePO_4$ Evidenced by In-Lab XPS. *J. Phys. Chem. C* **2010**, *114* (41), 17995-18000.

(32) Love, C. T.; Korovina, A.; Patridge, C. J.; Swider-Lyons, K. E.; Twigg, M. E.; Ramaker, D. E. Review of $LiFePO_4$ Phase Transition Mechanisms and New Observations from X-Ray Absorption Spectroscopy. *J. Electrochem. Soc.* **2013**, *160* (5), A3153.

(33) Hsu, K.-F.; Hu, S.-K.; Chen, C.-H.; Cheng, M.-Y.; Tsay, S.-Y.; Chou, T.-C.; Sheu, H.-S.; Lee, J.-F.; Hwang, B.-J. Formation Mechanism of $LiFePO_4$/C Composite Powders Investigated by X-Ray Absorption Spectroscopy. *J. Power Sources* **2009**, *192* (2), 660-667.

(34) Haas, O.; Deb, A.; Cairns, E. J.; Wokaun, A. Synchrotron X-Ray Absorption Study of $LiFePO_4$ Electrodes. *J. Electrochem. Soc.* **2005**, *152* (1), A191.

(35) Brozek, C. K.; Ozarowski, A.; Stoian, S. A.; Dincă, M. Dynamic Structural Flexibility of Fe-MOF-5 Evidenced by ^{57}Fe Mössbauer Spectroscopy. *Inorg. Chem. Front.* **2017**, *4* (5), 782-788.

(36) Hirose, K.; Honma, T.; Doi, Y.; Hinatsu, Y.; Komatsu, T. Mössbauer Analysis of Fe Ion State in Lithium Iron Phosphate Glasses and Their Glass-Ceramics with Olivine-Type $LiFePO_4$ Crystals. *Solid State Commun.* **2008**, *146* (5), 273-277.

(37) Song, Y.; Xie, B.; Song, S.; Lei, S.; Sun, W.; Xu, R.; Yang, Y. Regeneration of $LiFePO_4$ from Spent Lithium-Ion Batteries via a Facile Process Featuring Acid Leaching and Hydrothermal Synthesis. *Green Chem.* **2021**, *23* (11), 3963-3971.

(38) Wang, X.; Chen, Z.; Han, Z.; Gai, H.; Zhou, J.; Wang, Y.; Cui, P.; Ge, J.; Xing, W.; Zheng, X.; Huang, M.; Jiang, H. Manipulation of New Married Edge-Adjacent Fe_2N_5 Catalysts and Identification of Active Species for Oxygen Reduction in Wide pH Range. *Adv. Funct. Mater.* **2022**, *32* (18), 2111835.

(39) Yang, X.; Xia, D.; Kang, Y.; Du, H.; Kang, F.; Gan, L.; Li, J. Unveiling the Axial Hydroxyl Ligand on FeN_4C Electrocatalysts and Its Impact on the pH-Dependent Oxygen Reduction Activities and Poisoning Kinetics. *Adv. Sci.* **2020**, *7* (12), 2000176.

(40) Hammer, B.; Norskov, J. K. Why Gold Is The Noblest of All The Metals. *Nature* **1995**, *376* (6537), 238-240.

(41) Cheng, X.; Yang, J.; Yan, W.; Han, Y.; Qu, X.; Yin, S.; Chen, C.; Ji, R.; Li, Y.; Li, G.; Li, G.; Jiang, Y.; Sun, S. Nano-Geometric Deformation and Synergistic Co Nanoparticles—Co-N_4

Composite Sites for Proton Exchange Membrane Fuel Cells. *Energy Environ. Sci.* **2021**, *14* (11), 5958-5967.
(42) Ao, X.; Zhang, W.; Li, Z.; Li, J.-G.; Soule, L.; Huang, X.; Chiang, W.-H.; Chen, H. M.; Wang, C.; Liu, M.; Zeng, X. C. Markedly Enhanced Oxygen Reduction Activity of Single-Atom Fe Catalysts *via* Integration with Fe Nanoclusters. *ACS Nano* **2019**, *13* (10), 11853-11862.
(43) Hu, S.; Ni, W.; Yang, D.; Ma, C.; Zhang, J.; Duan, J.; Gao, Y.; Zhang, S. Fe_3O_4 Nanoparticles Encapsulated in Single-Atom Fe–N–C towards Efficient Oxygen Reduction Reaction: Effect of The Micro and Macro Pores. *Carbon* **2020**, *162*, 245-255.